

Design and Implementation of Semiconductor Photoconductive Switch for High Frequency Applications

Timur Abdilov

R11848908

Texas Tech University

Department of Electrical & Computer Engineering

May 2025

Acknowledgments

Acknowledgement is given to the Texas Tech University Electrical and Computer Engineering (ECE) Department for creating a curriculum that provides hands-on experience through ECE 3337 Electromagnetics Project. Appreciation is extended to Professor Jacob C. Stephens for his mentorship and guidance during the design and assembly stages of the project. Dr. Mohammad Saed and Dr. Jacob C. Stephens both made me interested in Electromagnetics, particularly high-power microwave and THz engineering. Gratitude is also expressed to Texas Tech University donors, whose contributions facilitated the establishment of the teaching lab and the stockroom in the ECE building, equipped with advanced industrial equipment. Additionally, recognition is given to Mr. Woodcock for efficient stockroom operations and logistics. Sincere gratitude is given to the members of the Pulsed Power Electronics and Ultrawide Bandgap Semiconductors Labs at Texas Tech University for their generous donation of semiconductor materials, which greatly contributed to the success of this project.

Abstract

This project focuses on the design and characterization of an optically controlled photoconductive microwave switch operating in the 1–4 GHz range (L and S bands). The switch is activated by High-Power LEDs (≤ 1 W optical power each) and is designed to meet strict performance criteria: insertion loss within ≤ 1 dB in the closed state and isolation $\geq 10\text{--}20$ dB in the open state. The final design is enclosed in shielded packaging for practical use and controlled via a designed external TTL gate driver for seamless integration into electronic systems.

To evaluate the switch's transient behavior, a custom measurement setup was developed to quantify switching dynamics with a target activation time below 100 μ s. The setup includes a logarithmic RF power meter (AD8317-based) to track power levels during switching events, 1-3GHz waveform generator, spectrum analyzer, complemented by a high-bandwidth oscilloscope and a VNA for precise rise-time and S-parameter analysis. The system allows real-time monitoring of power variations to ensure the switch meets speed and isolation requirements.

This project demonstrates a practical approach to photoconductive switching, balancing RF performance, optical efficiency, relative simplicity, and electronic control. The results provide a pathway for implementing fast, low-loss, and inexpensive microwave switching in applications requiring optical triggering and electrical isolation.

Contents

Acknowledgments	1
Abstract	2
Contents	3
List of Figures	4
List of Figures	4
1 Introduction	5
2 Part I	5
2.1 Semiconductors and Bandgap	5
2.2 Transmission Line Conductivity Modulation	6
3 Part II	8
3.1 Application Semiconductor PIN Photodiodes	8
4 Part III	9
4.1 Excitation Source and Conductivity Modulation	9
4.2 Excitation Wavelength Selection	11
4.3 Optical Excitation Device Assembly	13
4.4 Control of Optical Excitation with TTL Gate Driver	14
5 Part III	16
5.1 Silicon Based Microstrip Attenuator	16
5.2 Simulations of Photoconductive Switch in CST Studio	16
5.3 VNA characterization	18
5.4 Rise time characterization setup and measurements	19
6 Assembly Process	21
6.1 Manufacturing Methods	21
6.2 Direct Costs	21
7 Conclusion	23
7.1 Functionality	23
7.2 Safety, Public Health, and Welfare Considerations	23
7.3 Global, Social, Environmental, and Economic Factor	24
Bibliography	25
1 Appendix A	27
2 Appendix B	28
3 Appendix C	29

List of Figures

1	Intrinsic silicon lattice feauturing periodically spaced silicon (Si) atoms connected with covalent bonds $\approx 2.3\text{\AA}$	6
2	Transmission Line Equivalent Circuit Model [1]	7
3	Schematic of BPW34 based photoconductive switch in pataallel configuration	9
4	depth into silicon: Left - 405nm; Right - 490nm	12
5	depth into silicon: Left - 960nm; Right - 1100nm	12
6	Experimental measurements of penetration depth in Silicon [5]	13
7	LEDs: Left - Lumileds Luxeon; Middle - AMS Oslon Black; Right - Inolux C33	13
8	Optical Excitation Device: Left - Schematic; Right - Assembly	14
9	Modular Power Resistor Bank for Pulsed Power use	14
10	Gate driver circuit assembly	15
11	TTL gate driver circuit diagram	15
12	Photoconductive switch final prototype	16
13	Simulation of switch in closed state	17
14	Results of closed state simulations - S-parameters	17
15	Simulation of switch in open state	17
16	Results of open state simulations - S-parameters	18
17	S-parameters measured by VNA	19
18	Rise-time measurement routine flowchart	19
19	Full schematic representation of rise time measurement setup	20
20	Rise time measurements of 3GHz 0dBm wave; left - 5kHz pulses, right - 1kHz pulses	20
21	Spectrum Analyzer: left-2.8GHz LED OFF (closed state), right - 2.8GHz LED ON (open state)	21
22	Full DUT assembly	22
23	Budget sheet	22
24	Budget-time evolution graph Jan-May	23
25	Transmission Line Impedance Calculation Analytical tool CST Studio . .	27
26	Switching anomaly of 1.088 GHz wave being switched by 5kHz pulses . .	28
27	Switching anomaly of 1.21 GHz wave being switched by 5kHz pulses . .	28
28	Skills 1 Exam: Passed	29

1 Introduction

In high-power microwave frequency (mm-wave) applications, electrically controlled switches often present limitations due to parasitic effects, signal distortion, and potential breakdown under high voltage conditions. To mitigate these issues, it is preferable to implement switching mechanisms that provide electro-optical isolation, effectively decoupling the control signal from the microwave signal path.

One approach to achieving such isolation is through photoconductive switching, which leverages the ability of certain semiconductor materials to generate electron-hole pairs when exposed to light. By illuminating the semiconductor with a controlled optical source—such as an LED or laser—the material’s conductivity can be modulated, allowing the switch to transition between its open and closed states without direct electrical intervention. This method not only enhances reliability in high-power microwave systems but also enables fast, low-loss switching with minimal interference.

This project explores the design and implementation of an optically controlled photoconductive switch operating in the 1–4 GHz range, controlled by high-power state-of-the-art LEDs. The switch is evaluated for insertion loss, isolation, and transient response to ensure high-speed operation suitable for practical RF applications.

2 Part I

2.1 Semiconductors and Bandgap

Every semiconductor material, such as silicon (Si), has a well-defined electronic band structure consisting of a valence band and a conduction band, separated by a forbidden region known as the bandgap (E_g). Electrons in the valence band are bound to atoms (figure 1), while electrons in the conduction band are free to move, enabling electrical conductivity. For a semiconductor to transition from an insulating to a conductive state, electrons must gain enough energy to overcome the bandgap and transition from the valence band to the conduction band. For silicon (Si), the bandgap energy is $E_g=1.12$ eV at room temperature.

Using the equation of energy of a photon, we can determine the minimum photon wavelength required to excite an electron from the valence band to the conduction band:

$$E_\gamma = \frac{hc}{\lambda} \quad (1)$$

Where:

- h is Planck’s constant, $h = 6.626 \times 10^{-34}$ J · s
- c is speed of light in vacuum, $c = 2.998 \times 10^{-8}$ m · s⁻¹

If $1 \text{ eV} = 1.6 \times 10^{-19} \text{ J}$, Then:

$$1.12 \times 1.6 \times 10^{-19} = \frac{6.626 \times 10^{-34} \times 2.998 \times 10^{-8}}{\lambda} \quad (2)$$

From the relation above, for optical excitation of silicon, the required light source must have a wavelength shorter than $\lambda \approx 1108 \text{ nm}$ (i.e., higher energy photons). Suitable wavelengths include the near-infrared (NIR) and visible spectrum, such as 850 nm LEDs or lasers, commonly used in optically controlled semiconductor devices.

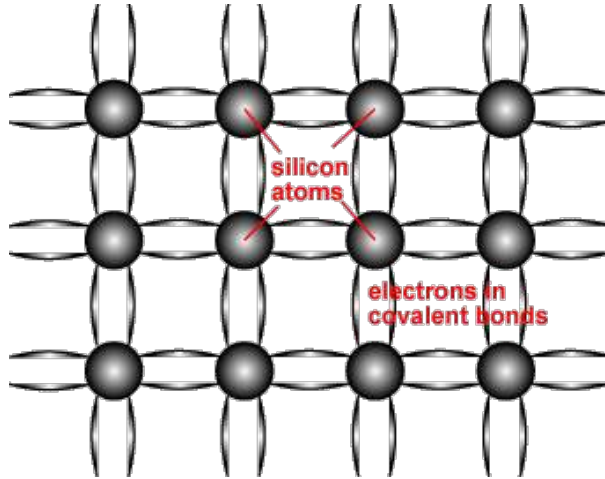


Figure 1: Intrinsic silicon lattice featuring periodically spaced silicon (Si) atoms connected with covalent bonds $\approx 2.3 \text{ \AA}$

Silicon was chosen as the semiconductor material for this project primarily due to its abundance and low cost, which make it a practical and widely accessible option for prototyping and production. Additionally, as mentioned above, silicon possesses a convenient bandgap of approximately 1.12 eV, corresponding to an absorption edge near 1100 nm. This makes it responsive to a broad range of optical excitation sources available on market, particularly in the visible and near-infrared spectrum.

Commercially available high power LEDs span a wavelength range from approximately 350 nm to 950 nm, which aligns well with silicon's absorption characteristics. This compatibility opens up flexibility in optical system design, allowing for a wide selection of off-the-shelf light sources for excitation and modulation in optoelectronic applications.

2.2 Transmission Line Conductivity Modulation

A transmission line is a structure designed to guide electromagnetic waves efficiently, characterized by its distributed parameters: series resistance (R), series inductance (L), parallel conductance (G), and parallel capacitance (C) per unit length. These parameters define the RLGC model (figure 2), which governs signal propagation along the line. The behavior of voltage and current along a transmission line is described by the Telegrapher's equations:

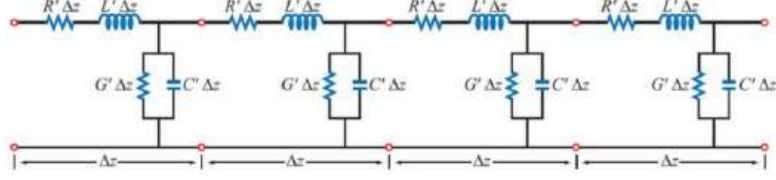


Figure 2: Transmission Line Equivalent Circuit Model [1]

$$\frac{\partial V(z, t)}{\partial z} = -(R + j\omega L)I(z, t) \quad (3)$$

$$\frac{\partial I(z, t)}{\partial z} = -(G + j\omega C)V(z, t) \quad (4)$$

where:

- $V(z, t)$ and $I(z, t)$ are the voltage and current at position z along the transmission line,
- R is the series resistance per unit length (Ω/m),
- L is the series inductance per unit length (H/m),
- G is the parallel conductance per unit length (S/m),
- C is the parallel capacitance per unit length (F/m),
- $\omega = 2\pi f$ is the angular frequency.

The characteristic impedance of the transmission line is given by:

$$Z_0 = \sqrt{\frac{R + j\omega L}{G + j\omega C}} \quad (5)$$

where:

- Z_0 is the characteristic impedance,
- R is the series resistance per unit length (Ω/m),
- L is the series inductance per unit length (H/m),
- G is the parallel conductance per unit length (S/m),
- C is the parallel capacitance per unit length (F/m),
- $\omega = 2\pi f$ is the angular frequency.

For an optically controlled photoconductive switch, we can modulate either the parallel conductance (G) or the series resistance (R) of the transmission line by illuminating a semiconductor.

- Increasing parallel conductance G (by generating free carriers via optical excitation) creates a low-impedance path, allowing signal transmission (closed state).
- Increasing series resistance R (by reducing carrier mobility or limiting conduction pathways) results in signal attenuation and reflection, effectively blocking transmission (open state).

By controlling these parameters dynamically, different switching behaviors—such as high-isolation, low-loss, or tunable attenuation—can be achieved, making photoconductive switches a powerful solution for RF and microwave applications.

It is important to note that the topology presented in this report is not the only viable approach for designing a photoconductive switch. In fact, the design methodology proposed here is relatively uncommon. Most existing research on photoconductive RF switches typically employs a different strategy—modulating a lumped element resistance. This is usually achieved by placing a photoconductive semiconductor material in the gap between conductors within a microstrip or coplanar waveguide structure.

While this approach is straightforward, it often suffers from significant parasitic insertion loss, even when the conductivity of the photoconductive material is strongly modulated under illumination. This makes it challenging to achieve low-loss switching behavior. For high-performance RF systems, a target insertion loss of less than 1 dB is often required, corresponding to an S21 (LOGMAG) between 0 and -1 dB. The approach taken in this work specifically aims to overcome these limitations by pursuing a topology that minimizes parasitic elements and improves switching efficiency.

3 Part II

3.1 Application Semiconductor PIN Photodiodes

One promising approach to photoconductive RF switching involves the use of PIN photodiodes, which are attractive due to their low cost, compact size, and fast optical response. Devices like the BPW34—a silicon PIN photodiode with a spectral response from 400 to 1100 nm and a rise time of approximately 100 ns—can act as optically controlled variable resistances or conductances [2][3]. When integrated in parallel with an RF transmission line, these diodes can shunt the signal to ground under illumination, effectively suppressing RF transmission and acting as a switch. In the test configuration, two BPW34 photodiodes were placed in opposing polarities to handle both signal polarities, and their conductance was optically modulated using high-power LEDs. This setup

demonstrated efficient switching behavior at frequencies up to approximately 20 MHz, validating the concept for low-to-mid-frequency RF applications.

$$X_c = \frac{1}{2\pi f C} \quad (6)$$

However, when operating at higher frequencies, particularly in the GHz range, significant performance degradation was observed. The primary limiting factor is the photodiodes' parasitic junction capacitance, which is approximately 70 pF at 0 V bias for the BPW34 [2]. At high frequencies, this capacitance presents a very low reactance (6), allowing RF energy to be undesirably shunted or reflected, resulting in poor signal integrity and high insertion loss. While PIN structures are generally designed to enhance photoconductive response by creating a large depletion region for efficient carrier generation, their inherent capacitance and package parasitics impose a practical upper frequency limit. For this reason, although they are well-suited for sub-20 MHz applications, alternative designs or specialized high-frequency photodiodes would be necessary for effective GHz-range switching.

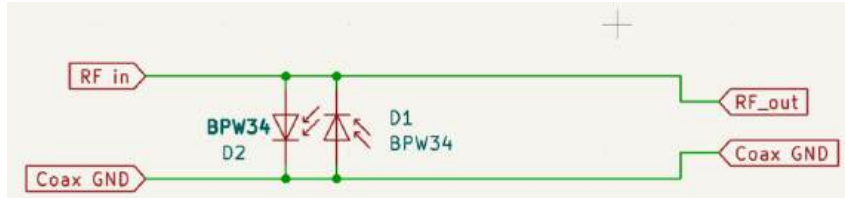


Figure 3: Schematic of BPW34 based photoconductive switch in parallel configuration

4 Part III

4.1 Excitation Source and Conductivity Modulation

The choice of excitation source is a critical aspect of this project, as it directly impacts the performance, efficiency, and feasibility of the photoconductive switching mechanism. For silicon-based devices, this typically corresponds to wavelengths ranging from approximately 350 nm (ultraviolet) to 950 nm (near-infrared). Within this range, commercially available LEDs provide a wide variety of options suitable for optical triggering. Manufacturers such as Lumileds, AMS Osram, Inolux, Vishay, Broadcom, and Cree LED offer high-performance, narrow- and wide-angle LEDs tailored for this spectral region. These components are readily accessible through major electronics distributors, including Digi-Key and Mouser Electronics.

These LEDs are available in diverse optical power ratings, packaging types, and emission profiles. In particular, dome-shaped lenses with different beam angles and focal

characteristics can be selected to optimize light coupling into the semiconductor switch. Choosing an appropriate excitation source not only ensures reliable switching behavior but also contributes to the overall robustness and scalability of the system.

$$\sigma = e(n_e\mu_e + n_h\mu_h) \quad (7)$$

In many practical semiconductor materials, the carrier mobilities (μ_e, μ_h) remain relatively constant under low to moderate excitation levels, meaning the conductivity is primarily governed by the carrier concentrations[1]. When a semiconductor is illuminated with photons of energy greater than or equal to its bandgap, electron-hole pairs are generated, leading to an increase in both n_e and n_h , and thus in conductivity—a phenomenon known as photoconductivity.

To optimize the performance of a photoconductive switch, careful management of the carrier population is essential. In the "off" state of the switch (i.e., when minimal conductivity is desired to reduce insertion loss), it is critical to minimize the number of photogenerated carriers. This can be effectively achieved by enclosing the Device Under Test (DUT) in a shielded, dark enclosure, preventing ambient light from inadvertently exciting the semiconductor.

Conversely, in the "on" state, where maximum attenuation and impedance mismatch are desired, the goal is to maximize the generation of electron-hole pairs. This is achieved by illuminating the semiconductor with a high-intensity optical source at a wavelength well-matched to the material's absorption spectrum. The generation rate (G) of carriers under illumination can be approximated by:

$$G = \eta\alpha(1 - R)\frac{P_\gamma}{h\nu A} \quad (8)$$

where:

- η is the quantum efficiency of the material
- α is the absorption coefficient of the semiconductor (silicon)
- R is the reflection coefficient of the material's surface
- P_γ is the optical power incident
- $h\nu$ is the incident photon energy,
- A is the illuminated area.

By examining the generation rate formula (8) and momentarily setting aside material-dependent parameters such as reflectivity and quantum efficiency for now, a clear design

trade-off emerges. The generation rate G , which determines the concentration of photo-generated electron–hole pairs, is directly proportional to the incident optical power P_γ and inversely proportional to the photon energy $h\nu$.

This implies that to maximize carrier generation, one should strive to maximize the optical flux (i.e., deliver as much power as possible using LEDs) while simultaneously minimizing the energy of each photon, thereby increasing the total number of incident photons per unit time. In practical terms, this favors the use of longer-wavelength light—just above the bandgap threshold—where each photon contributes to carrier generation without unnecessarily wasting energy as heat or other loss mechanisms. Therefore, for peak switching performance and efficient modulation, the ideal excitation wavelength should be just above the semiconductor’s bandgap, and the incident optical power should be as high as tolerable.

However, (8) accounts only for the generation of carriers on a thin surface layer of the semiconductor and does not reflect the volumetric behavior of carrier generation within the bulk of the material. To accurately model the photogeneration process in materials such as silicon, it is essential to incorporate the attenuation of light as it propagates through the semiconductor, which is governed by the absorption coefficient α . This leads to the concept of penetration depth, defined as $\delta = \frac{1}{\alpha}$.

The volumetric generation rate as a function of depth z into the material is given by:

$$G(z) = \alpha\Phi_\gamma \exp(-\alpha z) \quad (9)$$

Where Φ_γ is the photon flux density at the surface. This expression shows that carrier generation is not uniform, but instead decays exponentially with depth. Φ_γ is the photon flux density at the surface. This expression shows that carrier generation is not uniform, but instead decays exponentially with depth. Therefore, by maximizing the penetration depth—typically by selecting a wavelength closer to the material’s bandgap—the interaction volume between the light and the semiconductor increases, allowing photons to generate carriers deeper within the material.

4.2 Excitation Wavelength Selection

The absorption depth in silicon can be effectively modeled using the simulation tools provided by PV Education[4], which allow visualization of normalized carrier generation versus depth (z-direction) for various illumination wavelengths. Sweeping across common commercially available LEDs—such as 405 nm, 490 nm (or 488 nm), 530 nm (532 nm), 630 nm, 780 nm, 850 nm, and 950 nm—one can observe a clear and non-linear trend in absorption characteristics. Shorter wavelengths like 405 nm and 488 nm are absorbed almost entirely within the first few microns of the silicon surface (figure 4) due to their

high absorption coefficients, resulting in shallow generation profiles. In contrast, longer wavelengths such as 850 nm and 950 nm penetrate much deeper into the material (figure 5) before being significantly absorbed, generating carriers over a broader volume. This trend highlights the importance of wavelength selection in photoconductive applications, as it directly influences the spatial distribution of electron-hole pairs and overall device behavior under optical excitation.

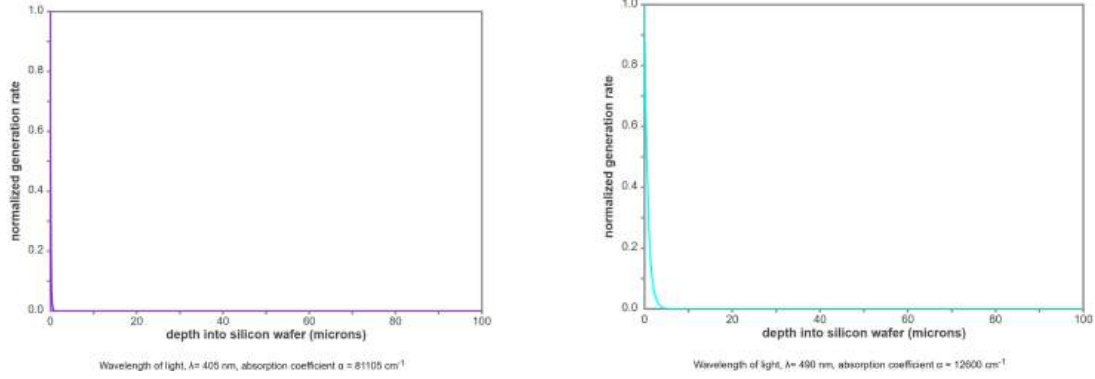


Figure 4: depth into silicon: Left - 405nm; Right - 490nm

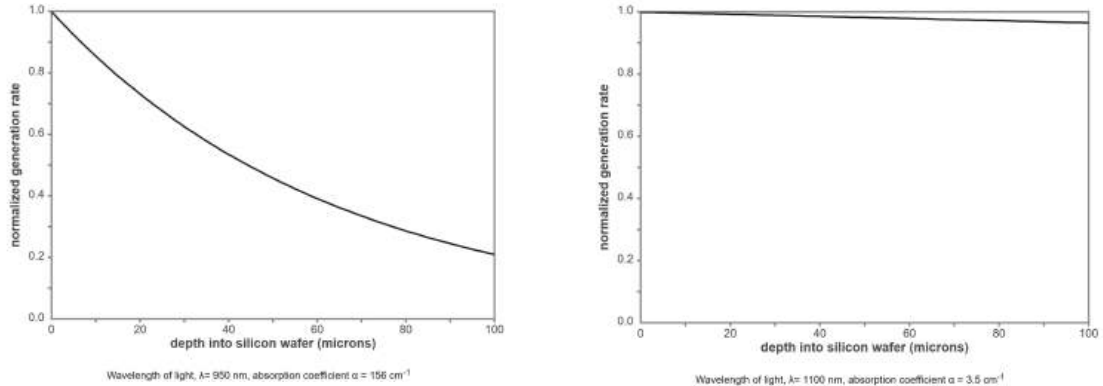


Figure 5: depth into silicon: Left - 960nm; Right - 1100nm

While NIR wavelengths offer deep penetration and effective volumetric carrier generation in silicon, wafer thickness must be considered. For typical wafer thicknesses (250–500 μm), wavelengths above 1050 nm may penetrate too deeply, causing a portion of the light to pass through the wafer without being absorbed, reducing efficiency. To ensure maximum photon–lattice interaction, it is preferred to use wavelengths with absorption depths matched to the material thickness. For optimal performance, target penetration depth is estimated to be in range 50–100 μm (figure 6).

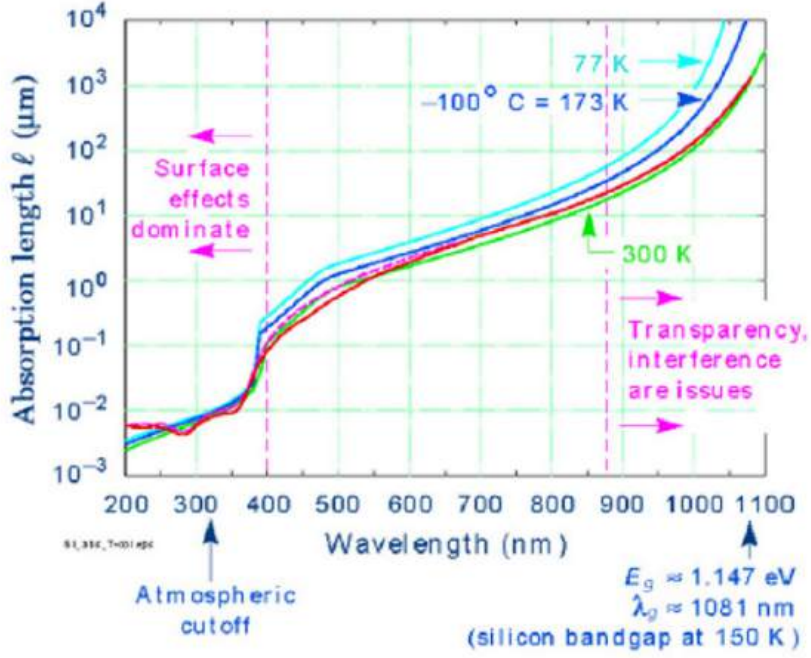


Figure 6: Experimental measurements of penetration depth in Silicon [5]

4.3 Optical Excitation Device Assembly

The real device assembly utilizes high-power infrared LEDs from manufacturers such as Lumileds, AMS Osram, Inolux, Vishay, Broadcom, and Cree LED, selected based on wavelength and optical performance. Due to physical constraints, the total LED array length is limited to approximately ± 40 mm, which allows for fitting 6 or 7 LEDs in the standard 3535 surface-mount package (figure 7). This package is commonly used for high-power IR LEDs, as it features a central thermal pad for effective heat dissipation.

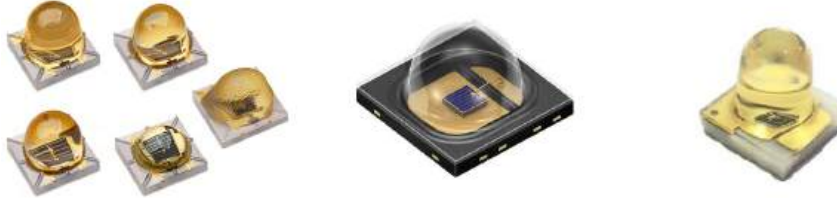


Figure 7: LEDs: Left - Lumileds Luxeon; Middle - AMS Oslon Black; Right - Inolux C33

Each LED typically operates at 0.7–1.3 A, delivering approximately 0.8–1.2 W [6][7][8] of optical output, though exact values vary by part. For current regulation, each LED is placed in series with a resistor, allowing the entire combination to be powered by a 5V supply, with resistor values chosen based on LED forward voltage and desired operating current according to datasheet specifications (figure 8).

During testing, half of the LEDs were paired with 20W power resistors to evaluate

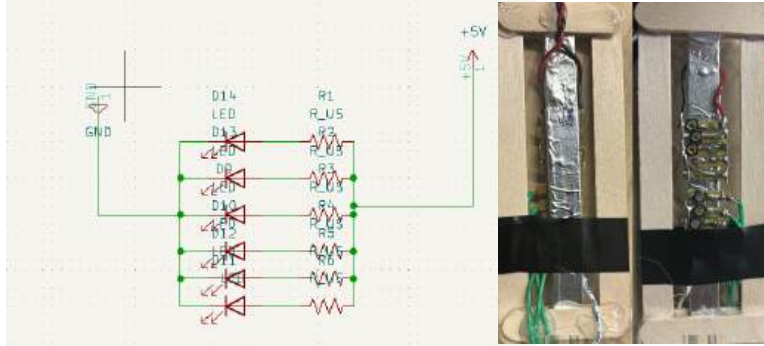


Figure 8: Optical Excitation Device: Left - Schematic; Right - Assembly

maximum lifetime performance (figure 9). For the remaining units, more compact ceramic SMD resistors rated at 0.5W were used to save space. Although these resistors are technically underspecified for continuous operation at full current, it is suspected they can tolerate short bursts of higher power without immediate degradation, making them suitable for pulsed or intermittent testing scenarios.



Figure 9: Modular Power Resistor Bank for Pulsed Power use

LEDs used in this project are capable of handling short high-current pulses, typically up to 3A for durations under $100\mu\text{s}$. Under these conditions, the emitted optical power can significantly exceed the rated continuous output specified in the datasheet, especially when the forward voltage across the array is increased. This overdrive operation is useful for generating brief, intense optical excitation. However, it should be noted that operating LEDs in this regime drastically reduces their lifetime.

4.4 Control of Optical Excitation with TTL Gate Driver

In this project, a square wave signal from a Keysight Trueform waveform generator is employed to control the excitation source. This signal is connected via a BNC interface to a gate driver circuit, which in turn controls the gate of an IRLZ44 MOSFET to modulate the current through the LED array. Directly interfacing the waveform generator with the MOSFET gate is suboptimal due to the generator's limited current drive capability and potential signal integrity issues, especially at higher frequencies or with longer interconnects.

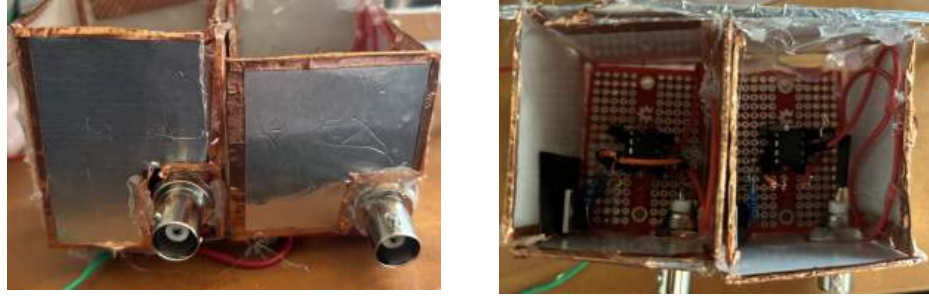


Figure 10: Gate driver circuit assembly

To address these challenges, the TC4420 high-speed MOSFET gate driver is utilized. The TC4420 is capable of delivering up to 6A [9] peak output current, ensuring rapid charging and discharging of the MOSFET's gate capacitance. This results in fast switching transitions, minimizing power losses and heat generation. The driver accepts TTL-compatible inputs, making it suitable for interfacing with standard waveform generators without the need for additional level-shifting circuitry.

The IRLZ44N MOSFET is selected for its logic-level gate drive capability, fully turning on with a gate-to-source voltage as low as 5V. It offers a low on-resistance, reducing conduction losses and improving overall efficiency. The combination of the TC4420 gate driver and the IRLZ44N MOSFET provides a robust solution for controlling high-current loads with precise timing and minimal power dissipation.

Initial testing involved applying square wave signals from the waveform generator to the gate driver circuit and observing the MOSFET's switching behavior. Measurements confirmed that the gate driver effectively amplified the control signal, enabling the MOSFET to switch fully on and off in response to the input waveform. This setup ensures reliable operation of the excitation source, with the gate driver providing necessary isolation and drive strength between the waveform generator and the power stage.

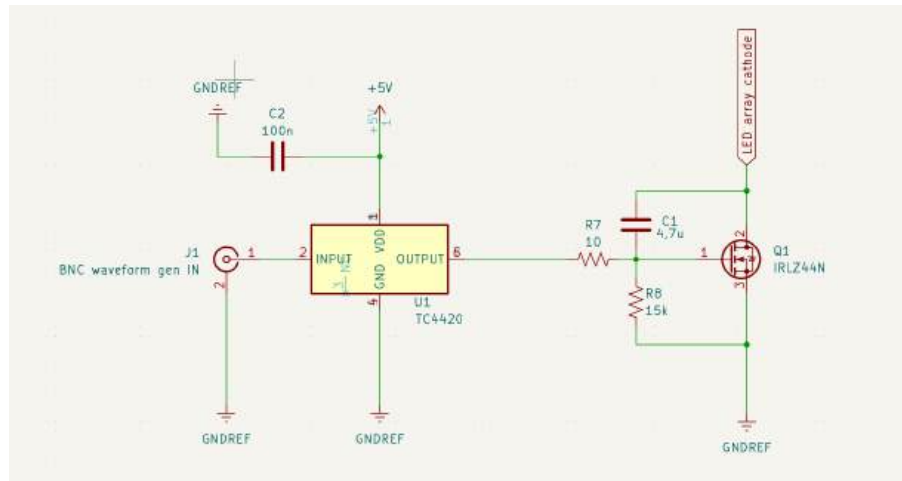


Figure 11: TTL gate driver circuit diagram

C2 serves as a decoupling capacitor, stabilizing the power supply to the TC4420,

while C1 is optional. Large resistor R18 acts as a gate pull-down resistor, ensuring the MOSFET remains off when the gate driver output is inactive.

5 Part III

5.1 Silicon Based Microstrip Attenuator

For this design, the motivation was drawn from a Pulsed Power and Power Electronics Lab publication [10] that explored the use of pure silicon in waveguides for similar applications, where silicon demonstrated good performance. In case of this project, silicon would serve as a dielectric on a small segment of the transmission line. When illuminated, this small section of silicon should undergo a change in conductivity, allowing it to act as a modulated resistance or conductance. This change in conductivity when illuminated would enable the control of the RF signal, effectively switching or modulating the signal path in the transmission line. The proven effectiveness of silicon in similar setups [11] makes it a strong candidate for achieving the necessary switching performance at GHz frequencies, and it offers the potential for more reliable, high-speed control than the previous approach with BPW34.

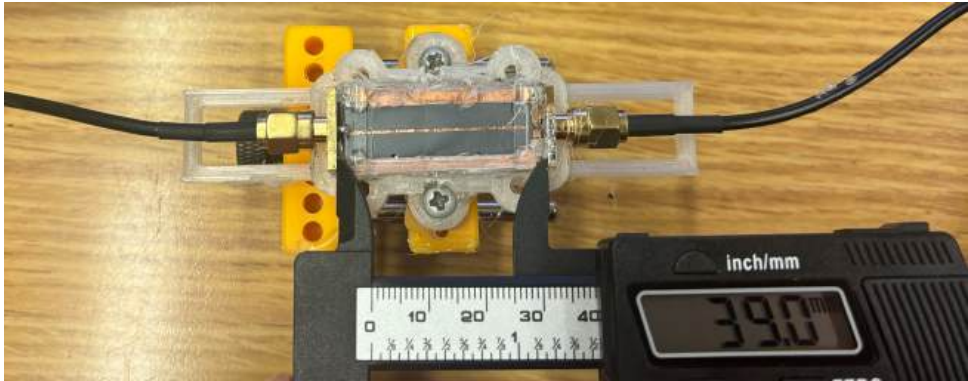


Figure 12: Photoconductive switch final prototype

5.2 Simulations of Photoconductive Switch in CST Studio

To ensure that the attenuator behaves as a well-matched transmission line in its normally closed (conductive) state, precise impedance matching to 50Ω was required. This was achieved by performing detailed microstrip dimension calculations using the embedded transmission line calculator in CST Studio (see Appendix A). These parameters formed the foundation for full 3D electromagnetic simulations within CST Studio, which confirmed field distribution, surface current behavior, and signal integrity across the operational frequency band.

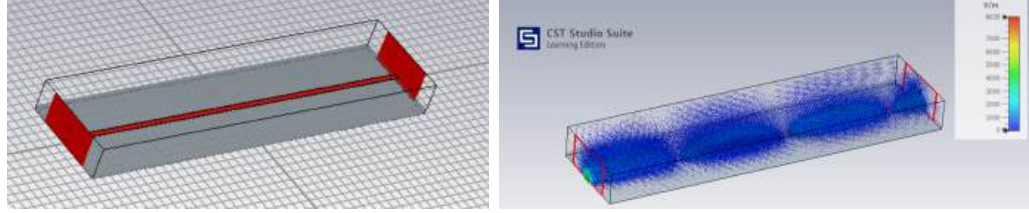


Figure 13: Simulation of switch in closed state

In CST Studio, a quasi-TEM mode was excited in the transmission line without inducing photoconductivity (figure 13). At 4 GHz, the field distribution indicated minimal attenuation, with the signal propagating effectively through the line.

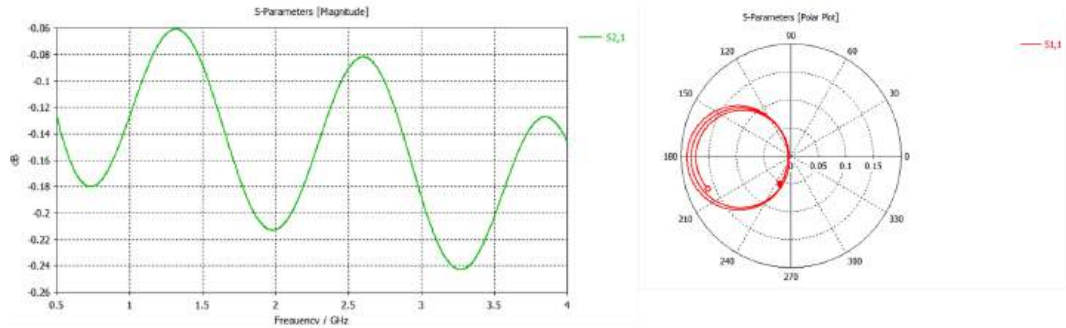


Figure 14: Results of closed state simulations - S-parameters

The S-parameter analysis showed an S21 attenuation of less than 1 dB, signifying low insertion loss. The Smith chart for S11 displayed traces primarily around the left semicircle, indicating a near-short circuit (figure 14).

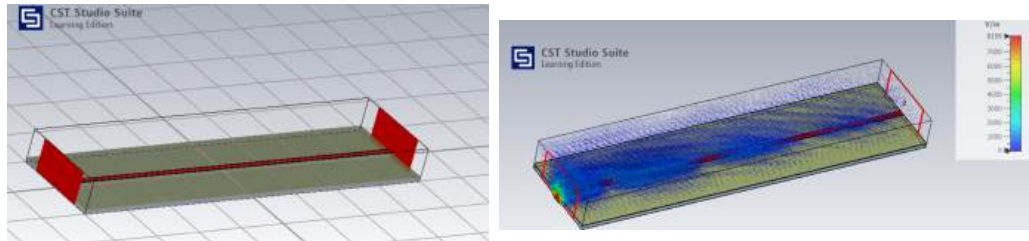


Figure 15: Simulation of switch in open state

To simulate the illuminated state of the photoconductive switch in CST, we model a thin $70\text{-}80\mu\text{m}$ surface layer of the silicon structure as a photoconductive material with a relative permittivity $\epsilon_r=11.9$, representing the optical penetration depth. This layer is assigned a conductivity value derived from estimated photogenerated carrier concentration, such as $\sigma \approx 100 \text{ S/m}$ under 7W of optical power (figure 15). With this configuration, CST simulations at 4 GHz show a noticeable decrease in electric field strength and distortion of field distribution along the transmission line, consistent with increased absorption and scattering due to carrier-induced loss (figure 16).

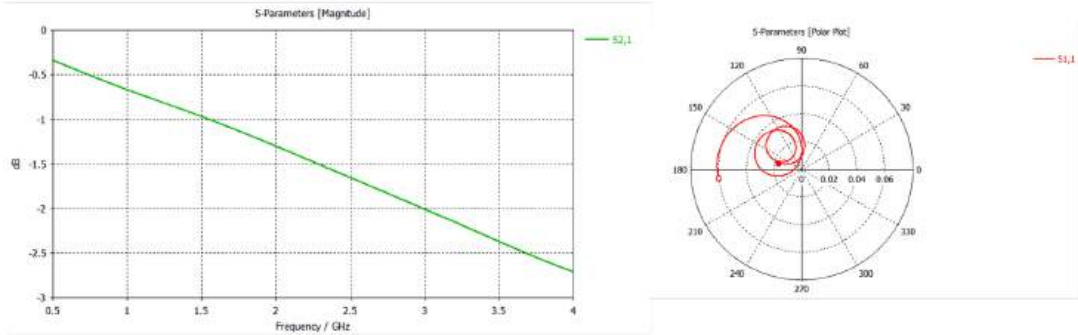


Figure 16: Results of open state simulations - S-parameters

The S-parameter analysis further confirms this behavior, with S21 attenuation exhibiting a linear trend across frequency, indicating a controlled and predictable signal attenuation.

5.3 VNA characterization

To evaluate the behavior of the photoconductive switch, a nanoVNA was used to measure both S11 and S21. The device was connected through 50Ω coaxial cables, and measurements were taken with and without optical excitation to capture how light-induced conductivity impacts signal transmission and reflection. Although both parameters were recorded, the performance evaluation primarily focused on the S21 results, which indicate how effectively the switch attenuates or transmits microwave signals. All measurement data were saved in .s1p and .s2p Touchstone formats, allowing for further analysis and visualization using VNA Saver (figure 17).

Based on the measurement results above, the blue trace represents the reference condition with no optical illumination, while the red trace corresponds to the illuminated state under high optical flux. As predicted, when no light is applied, the switch exhibits low insertion loss, remaining below 1dB across most of the measured frequency range. However, a localized resonance or anomaly is observed near 3.7GHz, where the insertion loss briefly increases to approximately -2.5 dB, potentially due to a structural or impedance mismatch effect.

In contrast, under illumination, the red trace shows a clear linear increase in attenuation with frequency, consistent with simulation predictions. This behavior indicates that the photoconductivity induced in the silicon effectively modulates the RF signal path. The slope of the S21 attenuation in the illuminated state is approximately -2.5 dB/GHz, highlighting a predictable and controllable signal degradation mechanism, suitable for dynamic RF switching applications.

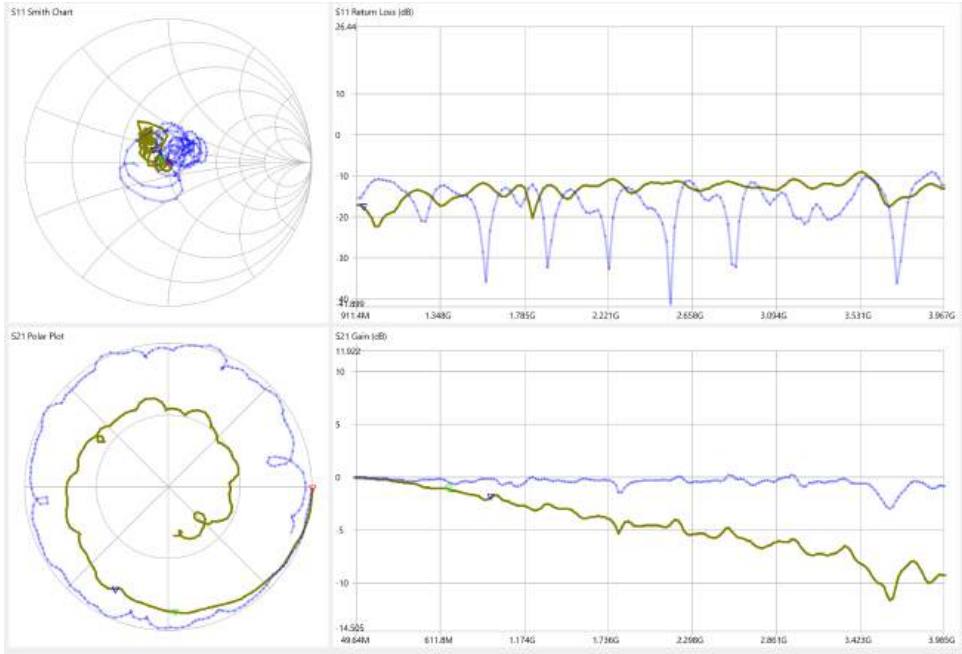


Figure 17: S-parameters measured by VNA

5.4 Rise time characterization setup and measurements

For rise-time characterization of the photoconductive switch, a Keysight EXG waveform generator was used to produce a continuous RF signal, which was delivered to the switch through a coaxial cable. The output of the switch was connected to an AD8317 logarithmic power detector evaluation board, which measures RF power in real time (figure 18, 19). The operating principle for rise-time measurement is based on the correlation between instantaneous output power and the degree to which the switch is conducting, since optical excitation modulates the switch's photoconductivity and thus its RF transmission.

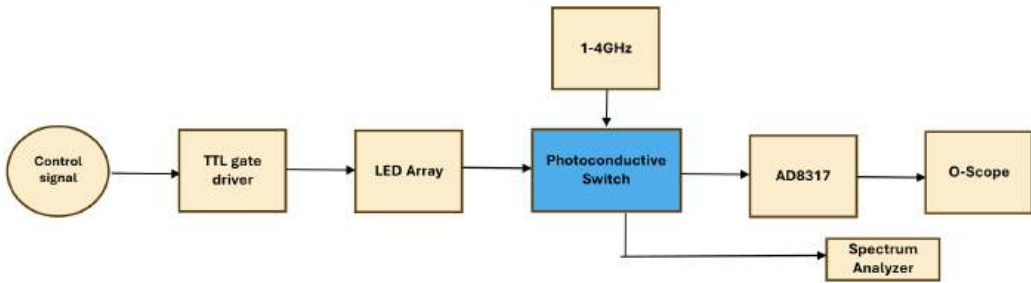


Figure 18: Rise-time measurement routine flowchart

The effective output power P_{out} can be related to the time-dependent transmission coefficient $T(t)$.

As the switch closes after illumination being removed, the transmission increases, causing a corresponding rise in output power detected by the AD8317. This voltage

output is monitored on an oscilloscope, representing the dynamic response of the switch.

For optical triggering, a Keysight Trueform function generator delivers square pulses to the MOSFET gate driver circuit, which consequently powers the LED array illuminating the switch. The reference control signal from the Trueform generator is also plotted on the oscilloscope to serve as a time reference. By comparing the time delay between the rising edge of the optical control pulse and the point where the AD8317 output stabilizes at its final level (or reaches a threshold), the rise time of the switch can be accurately estimated.

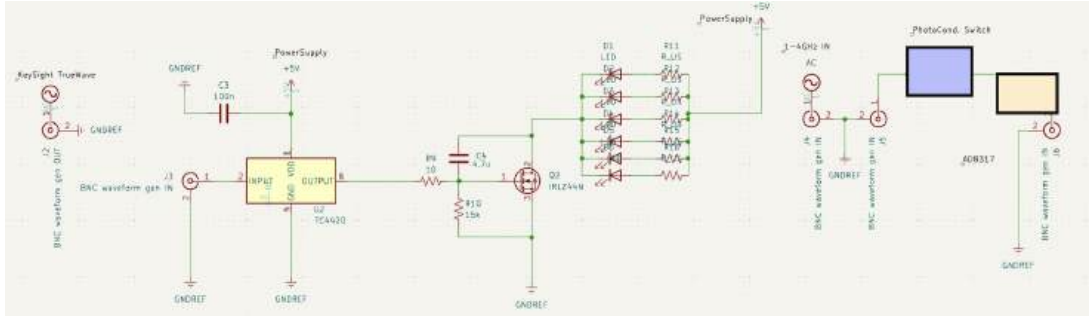


Figure 19: Full schematic representation of rise time measurement setup

The rise time of the photoconductive switch, as measured using the AD8317 power detector output, was found to be approximately 40–50 μ s across most of the tested frequency range (figure 20). However, at certain frequencies—notably around 1.088GHz—the output signal from the AD8317 displayed anomalous behavior, such as asymmetric rise and fall times or irregular transitions. These irregularities may be attributed to localized resonances, signal distortion, or nonlinear switching dynamics at those specific frequencies. For a detailed overview of these anomalies, refer to Appendix B, where additional oscilloscope waveforms are presented. A full dataset of the measurements is also available via the provided link. As the test frequency increases beyond 2 GHz, the switching response



Figure 20: Rise time measurements of 3GHz 0dBm wave; left - 5kHz pulses, right - 1kHz pulses

becomes more stable and symmetric, with rise and fall times being equal and exhibiting consistent behavior.

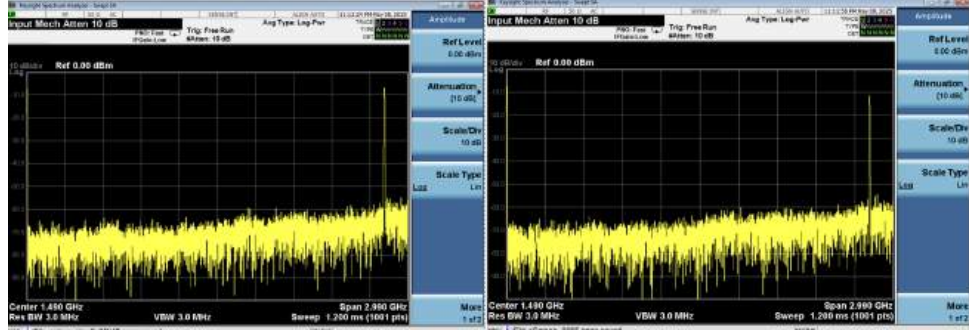


Figure 21: Spectrum Analyzer: left-2.8GHz LED OFF (closed state), right - 2.8GHz LED ON (open state)

6 Assembly Process

6.1 Manufacturing Methods

During the manufacturing process, the 0.4mm-wide microstrip conductor was manually cut from thin copper sheet stock to serve as the top transmission line (figure 10). Silicon chips with 111 crystal orientation used as the photoconductive medium were sourced from University Wafer. The switch incorporates two black SMA 50Ω connectors, manufactured by SparkFun, which serve as RF input and output ports.

For precise alignment within the housing, the entire switch copper bed assemble was mounted on a rigid translation stage, enabling fine positional adjustment. The main encasement was fabricated using 3D printing, and its exterior was lined with iron sheets for shielding purposes. To minimize electromagnetic interference, the AD8317 evaluation board was enclosed in its own shielded compartment, while the power resistor bank was similarly shielded and electrically grounded for noise suppression.

For improved usability, screw-in sockets were installed to facilitate easy connections. To enhance optical efficiency, the inner surface of the encasing lid was covered with mirrors, reflecting scattered light back onto the silicon surface to boost carrier generation. The TC4420 gate driver circuit was also housed in a separate shielded compartment mounted underneath the encasement, further isolating high-speed control circuitry from the RF path and minimizing crosstalk and parasitic coupling during operation.

6.2 Direct Costs

The direct costs for this project are primarily composed of the hourly wages of two engineers involved in the design, testing, and implementation phases. Additionally, the budget covers the expenses for various components used in the device's fabrication. Equipment rental costs have not been factored in yet. Overall, budget allocation is designed to ensure that all essential resources are available while maintaining cost-efficiency through-

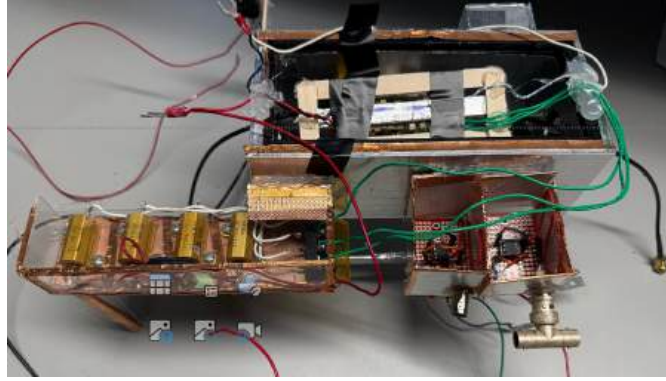


Figure 22: Full DUT assembly

out the project's development. The table below (figure 23) provides a clear context of the current state of the project in terms of budget spent and planned. Expensive ma-

Task	Description	Status	Planned Start Date	Actual Start Date	End Date	Labor			Materials			Overhead			Balance			
						Hrs	Wk	Total Labor	Units	Spares	Total Materials	Travel	Equipment / Space	Mile...	Budget	Actual	Unexpended	
Project 1																		
COPCO Control	SPIRCA Silicon photodiodes	Completed	01/29/28	01/29/28	7.0	\$40.00	\$280	0.0	\$1.00	\$0					\$ 100	\$ -	\$ 100	
max4238NT	Power integrated	Completed	01/29/28	01/29/28	7.0	\$40.00	\$280	1.2	\$1.00	\$0					\$ -	\$ -	\$ 0	
Logarithmic DAC	4K Power driver	Completed	01/29/28	01/29/28														
Driver	amplifier	Completed	02/03/28	02/03/28	7.0	\$30.00	\$210	2.0	\$0.00	\$0					\$ -	\$ -	\$ -	
LEDs	LEDs	Completed	02/03/28	02/03/28														
Logarithmic driver	DC Driver Amp (AD8017)	Completed	02/03/28	02/03/28											\$ 200	\$ -	\$ 200	
Waveform generator	DC driver	Completed	02/03/28	02/03/28														
Control	Other enhancement	Completed	02/03/28	02/03/28														
TS-Q2F4	Q2F4 Driver	Completed	02/03/28	02/03/28											\$ -	\$ -	\$ -	
Fox City 8.0	100A Bridge & Inverter	Completed	02/03/28	02/03/28	7.0	\$30.00	\$210	4.2	\$0.00	\$0					\$ -	\$ -	\$ -	
Subtotal						\$ 460		\$256	50	\$1	\$0	\$0	\$0	\$0	\$ 1,400	\$ 1	\$ 324	
User to complete non-physical costs only:																		
Task	Description	Status	Planned Start Date	Actual Start Date	End Date	Labor			Materials			Overhead			Balance			
						Hrs	Wk	Total Labor	Units	\$/Units	Total Materials	Travel	Equipment / Space	Mile...	Budget	Actual	Unexpended	
Project 2																		
TS-Q2F4	Power modules	Completed	02/19/28	02/19/28	7.0	\$40.00	\$280	0.0	\$1.00	\$0					\$ 100	\$ -	\$ 100	
TS-Q2F4	TO4400	Completed	02/19/28	02/19/28	7.0	\$40.00	\$280	0.0	\$1.00	\$0					\$ -	\$ -	\$ 0	
TS-Q2F4	HEC1 work	Completed	02/19/28	02/19/28														
SMPS-Main	coaxiles for DUT connector	Completed	02/19/28	02/19/28	7.0	\$20.00	\$140	2.0	\$1.00	\$0					\$ 100	\$ -	\$ 100	
TE-Cards	PCB	Completed	02/19/28	02/19/28	7.0	\$30.00	\$210	3.8	\$1.00	\$0					\$ -	\$ -	\$ 0	
Optical	LEDs High power	Completed	02/19/28	02/19/28											\$ -	\$ -	\$ 0	
Mask Works	3D-Alt-Fabricated Parts	Completed	02/19/28	02/19/28	7.0	\$30.00	\$210	0.0	\$1.00	\$0					\$ -	\$ -	\$ 0	
Encapsulation	3D part	Completed	02/19/28	02/19/28											\$ -	\$ -	\$ 0	
Total																		
Subtotal						\$ 240		\$160	50	\$1	\$0	\$0	\$0	\$0	\$ 2,400	\$ 1	\$ 340	

Figure 23: Budget sheet

terials, including silicon, were generously donated by members of the Pulsed Power and Power Electronics (P3E) and Ultrawide Bandgap Semiconductors Labs at Texas Tech University. Most of the project expenditures occurred between March and April (figure 24), primarily due to the purchase of high-power LEDs, which represent the largest single cost component of the system. Approximately \$186 were spent for purchasing components and materials. Estimated cost of manufacturing of a single device is around \$50.

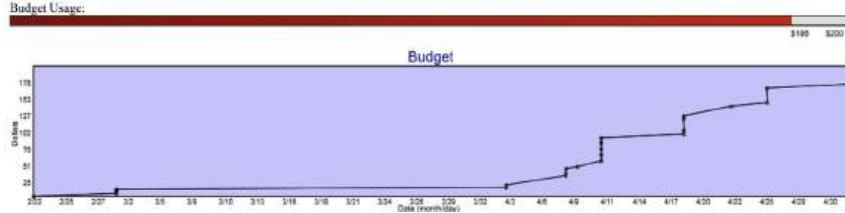


Figure 24: Budget-time evolution graph Jan-May

7 Conclusion

7.1 Functionality

This project explored optically controlled switching for GHz-range signals using both custom pure silicon-based and BPW34 photodiode-based systems. While the BPW34 performed well at lower frequencies, its parasitic capacitance caused impedance issues at higher frequencies. In contrast, the silicon-based photoconductive switch led to the successful development of a photoconductive attenuator, with performance that scales with frequency. At 4GHz, the switch achieved 10dB of attenuation, with highly predictable behavior across the L- and S-band ranges and a rise/fall times of 40-50 μ s. The design demonstrates a clear advantage over traditional gap-based approaches, offering greater consistency, broadband tunability, and low-cost fabrication. These results confirm the strong potential of silicon-based photonic structures for high-frequency microwave applications. Future efforts will focus on optimizing optical power delivery using flat lenses (i.e., Fresnel, metalens), thermal management, impedance matching, and advanced fabrication using semiconductor foundry facilities and CNC machining.

7.2 Safety, Public Health, and Welfare Considerations

Safety, health, and welfare are top priorities throughout the project. Work is conducted in a teaching lab that meets industrial safety standards, including 24/7 video surveillance, emergency supplies (AED and first aid kits), fire prevention, and advanced equipment such as Keysight oscilloscopes, VNA's, Spectrum Analyzers, and Waveform Generators. All participants are required to complete appropriate training to be able to react swiftly in case of emergency.

In this project, strict lab safety rules are enforced. It is prohibited to work in the lab wearing open-toed shoes or shorts. Particular safety protocols consist of:

- Protective Equipment (PPE): When working with electrical components, safety goggles, gloves, and appropriate clothing must be worn to prevent injury.
- Wire Handling: Take caution when stripping and clipping wires to prevent damage. To avoid cuts, the right instruments are used, and sharp edges are controlled.

- Fire Hazards: The use of power-consuming devices requires careful handling due to the risk of fire hazards. Devices such as soldering irons must be inspected for any damage before use.
- Optical Safety: All high-intensity optical components must be operated within isolated or enclosed systems. In scenarios where direct exposure cannot be fully avoided, protective eyewear must be worn at all times.

Fire extinguishers rated for electrical fires are readily accessible, and all participants are informed in safety protocols to prevent accidents.

7.3 Global, Social, Environmental, and Economic Factor

The development and utilization of photoconductive switches play a crucial role in advancing high-frequency telecommunications, enabling faster and more reliable data transmission. As the demand for high-speed communication networks grows, photoconductive switches facilitate the transition to higher frequency bands, supporting the expansion of next-generation wireless infrastructure and satellite communications. As an example, this technological progress enhances economic efficiency by improving the responsiveness of financial markets, global trade, and real-time data exchange.

Furthermore, research in photoconductive switching directly contributes to the growth of the semiconductor industry, driving innovations in material science, fabrication techniques, and circuit design. The continuous push for more efficient and high-speed switching devices fuels advancements in semiconductor manufacturing, fostering economic development and job creation in high-tech sectors.

The global energy mix also includes nuclear power and renewable energy sources like solar, wind, and hydroelectric power, but fossil fuels still have a disproportionate amount of influence in many areas. In the US, utility-scale electricity generation facilities generated an estimated 4.18 trillion kWh (4,178 billion kWh) of electricity, with fossil fuels such as coal, natural gas, and petroleum accounting for 60% of this power generation share [12]. From an environmental perspective, the design of more efficient photoconductive switches has the potential to reduce energy consumption in high-frequency systems. By minimizing power losses and optimizing switching performance, these devices can lower the overall energy demand of communication networks and electronic infrastructure. In turn, this could contribute to reducing the environmental impact associated with energy generation, such as greenhouse gas emissions from fossil fuel-based power plants.

Bibliography

- [1] F. T. Ulaby, *Fundamentals of Applied Electromagnetics*, 2001 Media ed. Upper Saddle River, NJ: Prentice Hall, 2001.
- [2] Vishay Semiconductors, “BPW34, BPW34S Silicon PIN Photodiode,” Rev. 2.1, 23-Aug-11. [Online]. Available: <https://www.vishay.com/docs/81521/bpw34.pdf>. [Accessed: Mar. 26, 2025].
- [3] D. Vovchuk, A. Mikhailovskaya, D. Dobrykh, and P. Ginzburg, ”Dual-band electro-optically steerable antenna,” arXiv preprint arXiv:2301.00770, Jan. 2023. [Online]. Available: <https://arxiv.org/abs/2301.00770>
- [4] C. Honsberg and S. Bowden, “Optical Properties of Silicon,” PVEducation.org. [Online]. Available: <https://www.pveducation.org/pvcdrom/materials/optical-properties-of-silicon>
- [5] A. Ronzhin, Silicon Timing Response to Different Laser Light, FERMILAB-TM-2643-E, Fermi National Accelerator Laboratory, Batavia, IL, USA, Jan. 2017. [Online]. Available: <https://lss.fnal.gov/archive/test-tm/2000/fermilab-tm-2643-e.pdf>
- [6] ams OSRAM, OSLON Black SFH 4713B Datasheet, Version 1.3, Dec. 2024. [Online]. Available: <https://ams-osram.com/products/leds/ir-leds/osram-oslon-black-sfh-4713b>
- [7] Inolux Corporation, IN-C33(X)TOIR Series 3535 IR LED Datasheet, Version 1.2, May 13, 2019. [Online]. Available: <https://www.inolux-corp.com/details.php?i=252#Infrared-Emitter—Sensor>
- [8] Lumileds Holding B.V., LUXEON IR Domed Line Product Datasheet, Document DS191, Nov. 22, 2023. [Online]. Available: <https://lumileds.com/products/infrared-emitters/luxeon-ir-domed-line/>
- [9] Microchip Technology Inc., “TC4420/TC4429 6A High-Speed MOSFET Drivers,” 2021. [Online]. Available: <https://www.microchip.com/wwwproducts/en/TC4420>. [Accessed: Mar. 26, 2025].

- [10] A. T. Hewitt *et al.*, “Optically Activated In-Waveguide Semiconductor Attenuators for the Controllable Isolation of Ka-Band Microwaves,” *IEEE Transactions on Microwave Theory and Techniques*, vol. 70, no. 4, pp. 2217-2223, Apr. 2022, doi: 10.1109/TMTT.2022.3144214.
- [11] A. W. Pang, C. D. Gamlath, and M. J. Cryan, “An Optically Controlled Coplanar Waveguide Millimeter-Wave Switch,” *IEEE Microwave and Wireless Components Letters*, vol. 28, no. 8, pp. 669-671, Aug. 2018, doi: 10.1109/LMWC.2018.2840966.
- [12] U.S. Energy Information Administration, “U.S. Electricity Generation by Energy Source,” U.S. Energy Information Administration, Feb. 29, 2024. [Online]. Available: <https://www.eia.gov/tools/faqs/faq.php?id=427&t=3>. [Accessed: Mar. 24, 2025].

1 Appendix A

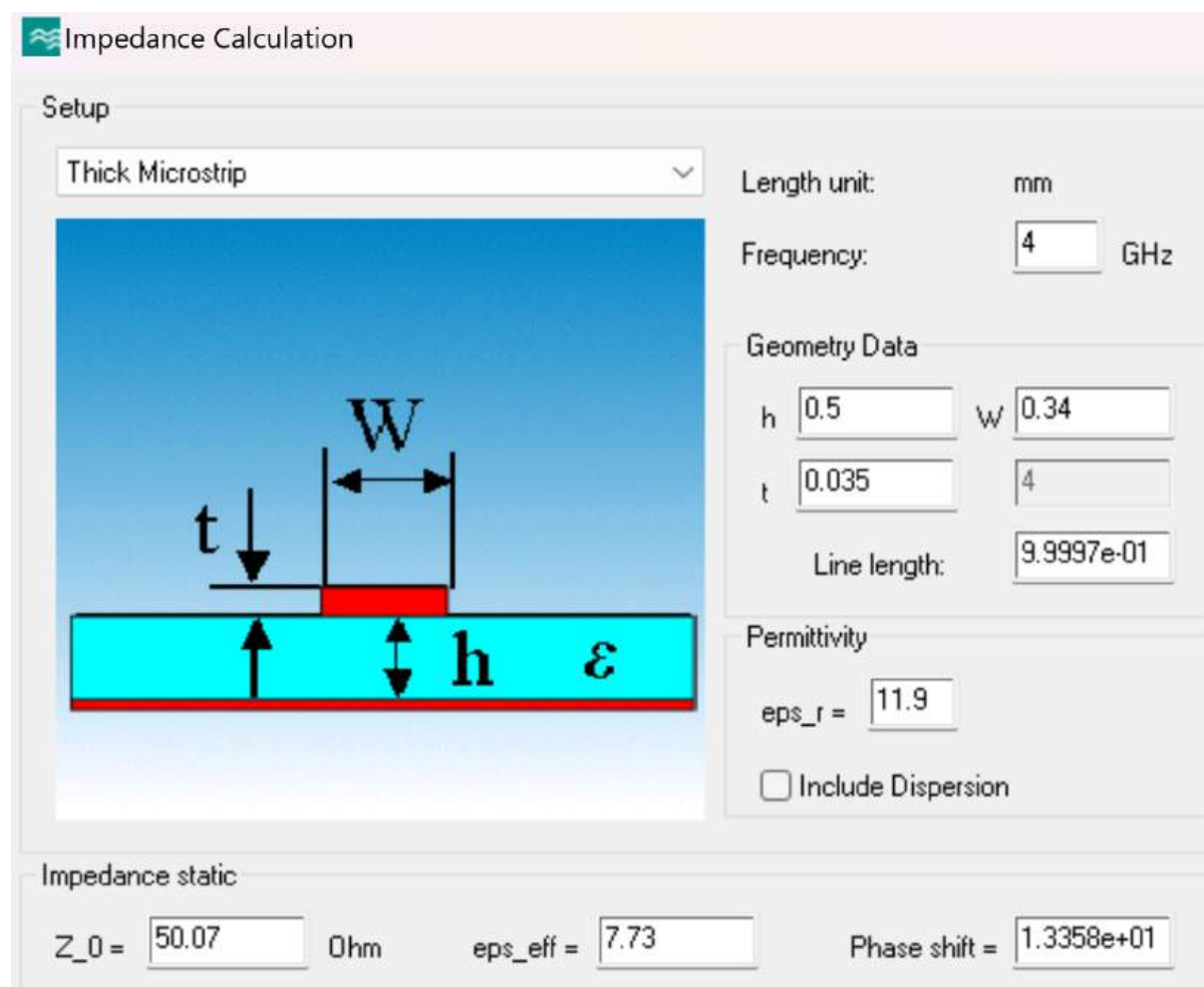


Figure 25: Transmission Line Impedance Calculation Analytical tool CST Studio

2 Appendix B

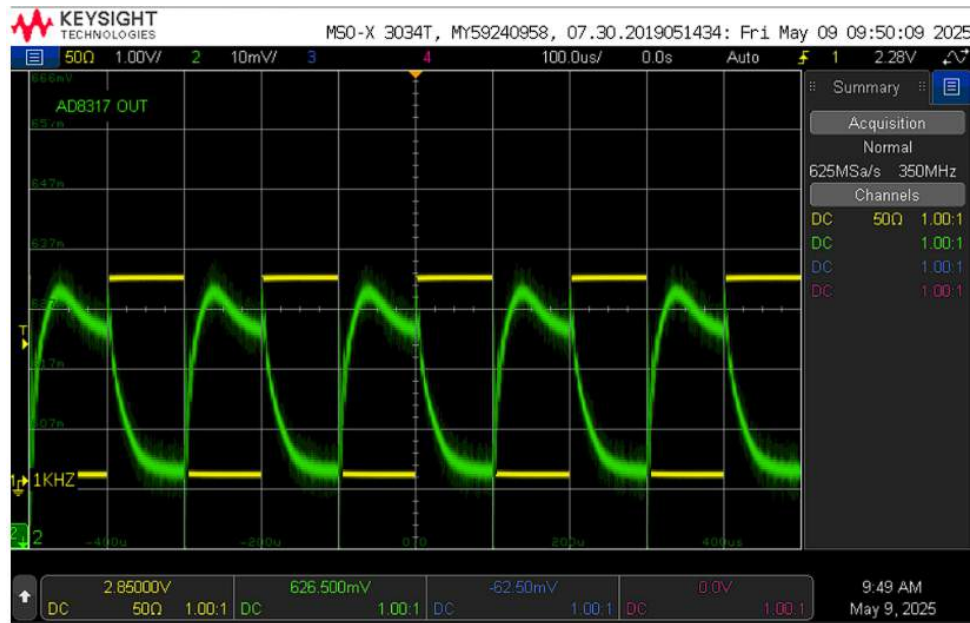


Figure 26: Switching anomaly of 1.088 GHz wave being switched by 5kHz pulses

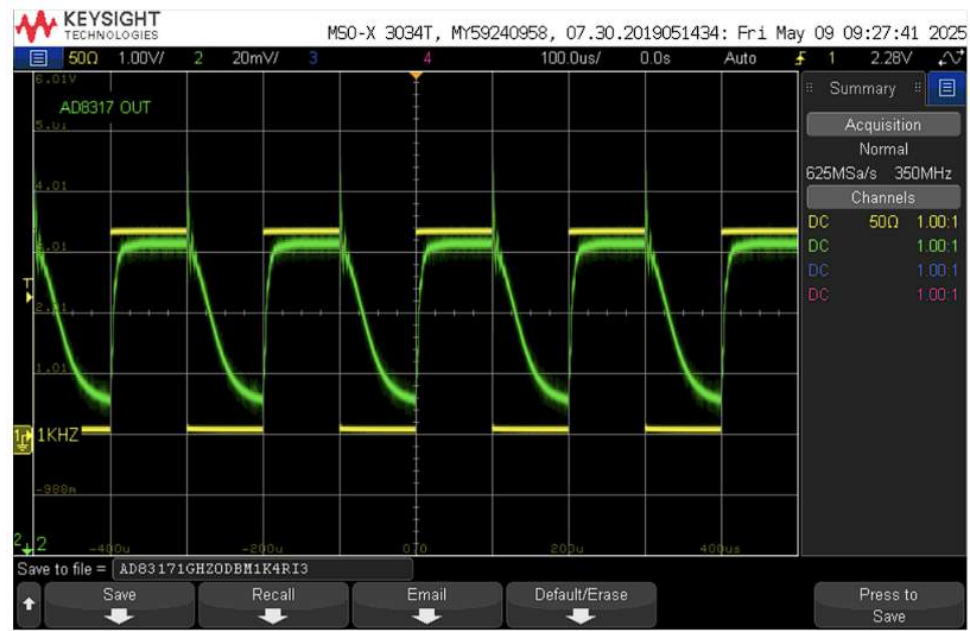


Figure 27: Switching anomaly of 1.21 GHz wave being switched by 5kHz pulses

Request more data via email: tabdilov@ttu.edu, or retrieve under link https://texastechuniversity-my.sharepoint.com/:f/g/personal/tabdilov_ttu_edu/Ehsck2fADvVNqe=neF27Q

3 Appendix C

Review Test Submission: Skills 1

User	Timur Abdikov
Course	ECE FE Exams: Seniors
Test	Skills 1
Started	4/30/25 9:17 PM
Submitted	4/30/25 10:28 PM
Status	Completed
Attempt Score	94 out of 100 points
Time Elapsed	1 hour, 10 minutes out of 3 hours
Results	Displayed
Feedback	Feedback

Figure 28: Skills 1 Exam: Passed